# Narrow absorption line Outflow in Seyfert 1 galaxy J1429+4518: Outflow's distance from the central source and its energetics

M. Dehghanian,[1] ⭐ N. Arav,[1] D. Byun[1] G. Walker[1] and M. Sharma[1]

[1]*Department of Physics, Virginia Tech, Blacksburg, VA 24061, USA*

## ABSTRACT

In the HST/COS spectrum of the Seyfert 1 galaxy 2MASX J14292507+4518318, we have identified a narrow absorption line (NAL) outflow system with a velocity of −151 km s$^{-1}$. This outflow exhibits absorption troughs from the resonance states of ions like C IV, N V, S IV, and Si II, as well as excited states from C II*, and Si II*. Our investigation of the outflow involved measuring ionic column densities and conducting photoionization analysis. These yield the total column density of the outflow to be estimated as log $N_H$=19.84 [cm$^{-2}$], its ionization parameter to be log $U_H$=-2.0 and its electron number density equal to log $n_e$= 2.75[cm$^{-3}$]. These measurements enabled us to determine the mass-loss rate and the kinetic luminosity of the outflow system to be $\dot{M}$=0.22 [$M_\odot$ $yr^{-1}$] and log $\dot{E}_K$=39.3 [erg s$^{-1}$], respectively. We have also measured the location of the outflow system to be at ∼275 pc from the central source. This outflow does not contribute to the AGN feedback processes due to the low ratio of the outflow's kinetic luminosity to the AGN's Eddington luminosity ($\dot{E}_K/L_{Edd}$ ≈ 0.00025%). This outflow is remarkably similar to the two bipolar lobe outflows observed in the Milky Way by XMM-Newton and Chandra.

**Key words:** galaxies: active –galaxies: Seyfert– galaxies: absorption lines – galaxies: individual: 2MASX J14292507+4518318

## 1 INTRODUCTION

Absorption outflows from active galactic nuclei (AGN) are frequently suggested as potential contributors to the AGN feedback processes. Various studies have discussed this idea, e.g. Silk & Rees (1998); Scannapieco & Oh (2004); Yuan et al. (2018); Vayner et al. (2021); He et al. (2022). Absorption lines found in the rest-frame UV spectra are typically grouped into three main categories based on their characteristics: broad absorption lines (BALs) which have a width of ≥2000 km s$^{-1}$, narrow absorption lines (NALs) with a width of ≤500 km s$^{-1}$, and a middle subgroup known as mini-BALs (Itoh et al. 2020). When it comes to BALs, it is clear that the absorbing gas is connected to the AGN (Vestergaard 2003) and could indeed have a noticeable impact on suppressing the star formation rate within the host galaxies (Chen et al. 2022); however, the nature of NAL outflows is less understood. This is due to the challenge of discerning intrinsic NALs (associated NALs) from those NALs that are unrelated to the quasars (intervening NALs). Intervening NALs can originate from various sources, including intervening galaxies, intergalactic clouds, Milky Way gas, or gas within the host galaxies of the quasars (Misawa et al. 2007a). Several studies (e.g. Misawa et al. (2007a); Chen & Qin (2013); Chen et al. (2018, 2020)) have highlighted the point that variations in the absorption lines serve as a robust indicator to distinguish between narrow absorption lines arising from the outflow system, or those called intervening NALs. These variations in absorption lines typically arise from changes in the column density of absorbing gas as part of the intrinsic mechanism.

Shen & Ménard (2012) and Chen et al. (2018) explain that a velocity of 3000 km s$^{-1}$ is often used to limit associated NALs; however, it should also be noted that some NAL outflows with velocity being obviously larger than 3000 km s$^{-1}$ have been observed (Hamann et al. 2011; Chen & Qin 2013). Using large samples of the SDSS quasar C IV and Mg II narrow-line absorptions, Chen & Pan (2017) discuss that the velocity boundary is associated with the quasar luminosity. In the study referred to, it is proposed that velocity thresholds of 4000 km s$^{-1}$ be used to identify quasar CIV-associated NALs and velocity thresholds of 2000 km s$^{-1}$ be employed to identify quasar MgII-associated NALs.

Despite the fact that NALs have received less attention than BALs, they hold great potential as a useful tool for investigating the physical properties of outflows because of these two significant reasons (Misawa et al. 2007b):

• NALs do not have the problem of self-blending, which is defined as blending blue and red components of doublets like C IV $\lambda\lambda$ 1548,1551Å.

• NALs appear in a larger variety of AGNs, whereas BALs are mostly detected in radio-quiet quasars.

This paper identifies and analyzes the NAL outflow system of the AGN 2MASX J14292507+4518318 (hereafter J1429+4518) using the observations performed by the Hubble Space Telescope (HST) in 2021. For this object, the intrinsic nature of the NAL is deduced from the presence of several excited state absorption narrow lines observed in the spectrum. The paper's structure is as follows: In the next Section, we described the observations and data acquisition of the target. It is followed by Section 3, which includes the analysis, and explains the methods used in the paper. Section 3 also

⭐ E-mail: dehghanian@vt.edu

details the approaches used to calculate the ionic column densities of the NALs. Calculations of the electron number density and location of the outflow, along with the best photoionization solution, are all included in Section 3. Part of Section 3 is dedicated to finding the central source's mass and the AGN's Eddington luminosity. These calculations are followed by estimating the energetics of the outflow system. Section 4 discusses the stability of the outflow and indicates the importance of the NALs in general. In this Section, we have also compared our NAL outflow system with two lobe outflows detected in the Milky Way. Finally, Section 5 gives a summary of what we have done here and concludes the paper.

Here we adopted a cosmology with h= 0.696, $\Omega$= 0.286, and $\Omega_\nu$ = 0.714 (Bennett et al. 2014). We used the Python astronomy package Astropy (Astropy Collaboration et al. 2013, 2018) for our cosmological calculations, as well as Scipy (Virtanen et al. 2020), Numpy (Harris et al. 2020), and Pandas (Reback et al. 2021) for most of our numerical computations. For our plotting purposes, we used Matplotlib (Hunter 2007).

## 2 OBSERVATIONS

J1429+4518 is a Seyfert 1 galaxy, located at Redshift z=0.07454, with J2000 coordinates at RA=14:29:25.07 and DEC=+45:18:31.93. The galaxy was observed using the HST Cosmic Origins Spectrograph (HST/COS) on three separate occasions: September 19th 2021, December 20th of 2021, and December 21st of the same year, as part of HST Proposal 16301 (Putman et al. 2020). The first observation utilized the G130M grating, while the subsequent two observations used G160. For this study, we excluded the observation taken on December 21st of 2021, as it covered the same wavelength range as the other December observation but had a shorter exposure time. The spectral data for both observations are displayed in Figs 1 and 2 .

After obtaining the relevant data from the Mikulski Archive for Space Telescopes (MAST), we detected an outflow at a velocity of v= –151 km s$^{-1}$, with blue-shifted ionic absorption lines denoted by red vertical lines in Figures 1 & 2. Among the identified absorption lines, several well-known resonance doublets, such as C IV and N V, were observed. Additionally, we identified absorption lines arising from excited states, such as C II* and Si II*.

### 2.1 Redshift considerations

The redshift assigned to the object (z=0.07454) is the sole value documented in the SIMBAD Astronomical Database [1] and is derived from optical data analysis. Despite the NASA/IPAC Extragalactic Database (NED)[2] reporting seven different redshift values (within the range of z=0.0745 to z=0.0748) for this object, their preferred redshift in their databases is also documented as 0.07454. Furthermore, the SDSS Science Archive Server (SAS)[3] confirms this redshift for the same object. In the interest of maintaining consistency with these databases, we have adopted the same redshift value. It is essential to acknowledge the inherent uncertainties associated with this value: To ensure that we have picked a reliable redshift and to mitigate the potential larger uncertainties associated with C IV emission line models (Chen et al. 2019; Shen et al. 2011), we opted to utilize the

[1] SIMBAD Astronomical Database: http://simbad.cds.unistra.fr/simbad/
[2] NED:https://ned.ipac.caltech.edu/
[3] SAS:https://dr18.sdss.org/

SDSS data directly and perform modeling on [O III]$\lambda$5007Å. For this purpose, we have used the optical spectrum obtained in March 2003 (MJD 52728) and used two Guassians to fit [O III] emission line. Our modeling yielded to a redshift of 0.0747, a value only 0.00016 larger than the NED estimate. However, this will increase the velocity of the outflow to be v= –195 km s$^{-1}$. Taking all these considerations into account, we utilize the initially assumed redshift throughout this paper, and we assume an uncertainty of $\Delta$v~44 km s$^{-1}$ when needed.

## 3 ANALYSIS

### 3.1 Ionic Column Densities

Determining the ionic column densities (N$_{ion}$) of the outflow absorption lines is crucial for understanding the physical properties of the outflow system. While there are two methods to estimate the ionic column densities, we employed "the apparent optical depth" (AOD) method for all detected absorption lines since all of the identified doublets appear to be saturated (see Sections 3.1.1). In this method, the main assumption is that the outflow uniformly and fully covers the source (Spitzer 1968; Savage & Sembach 1991). When using the AOD method, one can infer the column density via the equations 1& 2 below (Spitzer 1968; Savage & Sembach 1991):

$$I(\lambda) = I_0(\lambda)e^{-\tau(\lambda)}, \tag{1}$$

in which $I(\lambda)$ and $I_0(\lambda)$ are the intensities with and without the absorption, respectively. $\tau(\lambda)$ is the optical depth of the absorption trough. Then, the ionic column densities can be measured using equation 2 (Arav et al. 2001):

$$N_{ion} = \frac{3.7679 \times 10^{14}}{\lambda_0 f_{ik}} \times \int \tau(\nu) \, d\nu [cm^{-2}], \tag{2}$$

where $\lambda_0$ is the transition's wavelength and $f_{ik}$ is the oscillator strength of the transition. For more details regarding the AOD method, please see Arav et al. (2001), Gabel et al. (2003), and Byun et. al (2022c). The other method is called the partial covering (PC) method, and it will not be used in this paper. For a detailed explanation of both methods and to better understand the logic behind them and get a sense of their mathematics, please refer to Barlow et al. (1997); Arav et al. (1999a,b); de Kool et. al (2002); Arav et al. (2005); Borguet et al. (2012a); Byun et. al (2022b,c).

Below we explain how various absorption lines were treated and why we applied the AOD method approach in each case. For each absorption line that we were interested in, we used the redshift of the outflow (z$_{outflow}$) to transfer the spectrum from wavelength space to velocity space (please refer to Fig. 3). As shown by the dashed lines in Fig. 3, we have chosen a velocity range of -210 km s$^{-1}$ to -90 km s$^{-1}$ as our integration range when performing column density calculations. This region was chosen based on the centroid velocity and the absorption trough width of Si IV. Since all the absorption lines result from the same outflow system, we use the same integration range for all.

#### 3.1.1 C IV, Si IV, and N V doublets

The C IV $\lambda\lambda$1548, 1551Å, Si IV $\lambda\lambda$1394, 1403Å and N V $\lambda\lambda$1239, 1243Å absorption lines are prominent spectral features observed in AGN outflows. All of these lines are easily detectable in the spectrum of J1429+4518 (see Figs 1 and 2) indicating the presence of an absorption outflow system. However, while these lines are recognized

as doublets (and expected to be treated using the PC method), they are all very saturated as their blue-to-red trough ratio is very close to 1:1 for all three cases. For this reason, in our calculations, we adopted the AOD results of the red doublet (since it has the lower oscillator strength) and considered them a lower limit to the total ionic column density for each species. Note that for the case of N v, the high-velocity wing of the red doublet is actually Galactic C II $\lambda$1334Å absorption.

### 3.1.2 Ly$\alpha$

As shown in Fig. 3, Ly$\alpha$ is also suspected of being highly saturated since it has a very large optical depth. For this reason, while we use the AOD method to calculate its ionic column density, we take it as a lower limit and not an accurate measurement.

### 3.1.3 C II $\lambda$ 1334 Å and C II* $\lambda$ 1336 Å

Since these two lines are from different energy levels, we employ the AOD method to calculate the column density for each line individually. However, as depicted in Fig. 3, the flux ratio of C II to C II* appears to be approximately 1:1. While it is evident that the lines are not fully saturated (optical depth is not very large), a 1:1 ratio might have resulted from a mild saturation effect. For this reason, we proceed to utilize their column density resulted from the AOD method as a lower limit, not an accurate measurement. In later steps, we use the ratio of $\frac{N_{ion}(C\,II^*)}{N_{ion}(C\,II)}$ to extract a lower limit for the electron number density of the outflow.

### 3.1.4 Si III $\lambda$ 1206Å

As marked in Fig. 1, Si III $\lambda$ 1206Å is easily identifiable. Since this line is a singlet, we use our usual AOD method to infer its ionic column density. However, since it appears to be very deep (see Fig. 3) and hence probably saturated, we consider the results as a lower limit, not an actual measurement.

### 3.1.5 Si II $\lambda$1260 Å and Si II* $\lambda$1265 Å

Fig. 3 shows that both resonance and excited state absorption lines of Si II ion are detectable. Since the Si II trough is significantly shallower than the Si III trough, we cautiously accept its AOD measurement as a real measurement as opposed to a lower limit. The fact that Si II* is shallower than Si II suggests that we can use their ionic column densities ratio to estimate the electron number density of the outflow (Arav et al. 2018). Later in Section 3.3.1 we discuss this process in more detail.

### 3.1.6 S IV $\lambda$1063 Å and S IV* $\lambda$1073 Å

While we were able to accurately measure the column density of the S IV using the AOD method, S IV* is absent (Fig. 3). For this reason, we used a Gaussian fit based on the S IV absorption line and estimated an upper limit for S IV* ionic column density. Then the ratio of $N_{ion}$(S IV*) to $N_{ion}$(S IV) can be used to extract an upper limit for the electron number density of the outflow system.

Fig. 4 illustrates the Gaussian fit for both the resonance and excited states of the S IV line. It is important to note that we modeled the S IV* state using the best-fit parameters obtained for the S IV resonance line as the template. The depth of the curve for S IV* was allowed to adjust within a $3\sigma$ error range during the fitting process. We have checked

| Ion | AOD | Adopted |
|---|---|---|
| C IV | $580^{+50}_{-40}$ | $>580_{-122}$ |
| Si IV | $63^{+7}_{-6}$ | $>63_{-14}$ |
| Ly$\alpha$ | $105^{+2}_{-2}$ | $>105_{-21}$ |
| N v | $503^{+24}_{-31}$ | $>503_{-103}$ |
| C II | $187^{30}_{-27}$ | $>187_{-46}$ |
| Si II | $9^{+1}_{-1}$ | $9^{+1}_{-1}$ |
| Si III | $18^{+1}_{-1}$ | $>18_{-4}$ |
| S IV | $262^{+31}_{-29}$ | $262^{+61}_{-60}$ |
| Si II* | $4^{+1}_{-1}$ | $4^{+1}_{-1}$ |

**Table 1.** The ionic column densities of the absorption lines detected in the J1429+4518 outflow system. Please note that the reported/adopted value for C II includes the column densities of C II and C II*. We did not add the systematic error to Si II and Si II* since these two lines are only 5Å apart and will not be affected much by a systematic error. All of the column density values are in units of $10^{12}$ cm$^{-2}$.

the spectrum for any signs of the C III* $\lambda$ 1175Å narrow absorption line and we were not able to identify any traces of the mentioned line. Table 1 summarizes the results we got from our $N_{ion}$ measurements, along with the numbers we chose to use in the next step, which will assess the outflow characteristics. The adopted errors include the corresponding AOD errors and a systematic error (20% of the adopted value), which are quadratically added together (e.g. Xu et al. 2018; Miller et al. 2018, 2020c).

### 3.2 Photoionisation Solution

We calculated the ionic column densities of the mentioned absorption lines for the primary purpose of estimating the characteristics of the outflow, including the total hydrogen column density ($N_H$) and the ionization parameter of the system ($U_H$) (e.g. Xu et al. 2019; Byun et. al 2022a,b,c; Walker et. al 2022). To do so, we use Cloudy simulations (Ferland et al. 2017) in which a grid of $N_H$ and $U_H$ are used to predict the abundance of various ions. Then we constrain the $N_H$ and $U_H$ values based on our measured ionic column densities. The top panel of Fig. 5 shows the results of this process. To produce this Figure, we used the spectral energy distribution (SED) of AGN HE0238-1904 (hereafter HE0238, Arav et al. 2013) in Cloudy and set a large range of grids on $N_H$ and $U_H$. In Fig. 5-top panel, the coloured contours show the values labeled "adopted" in Table 1. As this Figure shows, a single-phase solution is sufficient to satisfy the constraints from the ionic column densities. Based on these results, we narrowed down the column density-ionization space to a pair of $N_H$ and $U_H$ for the absorption outflow system: $U_H = -2.0^{+0.1}_{-0.1}$ and $N_H = -19.84^{+0.20}_{-0.20}$ [cm$^{-2}$] (reduced $\chi^2 = 2.5$). Please note that to produce these results, a solar abundance was assumed.

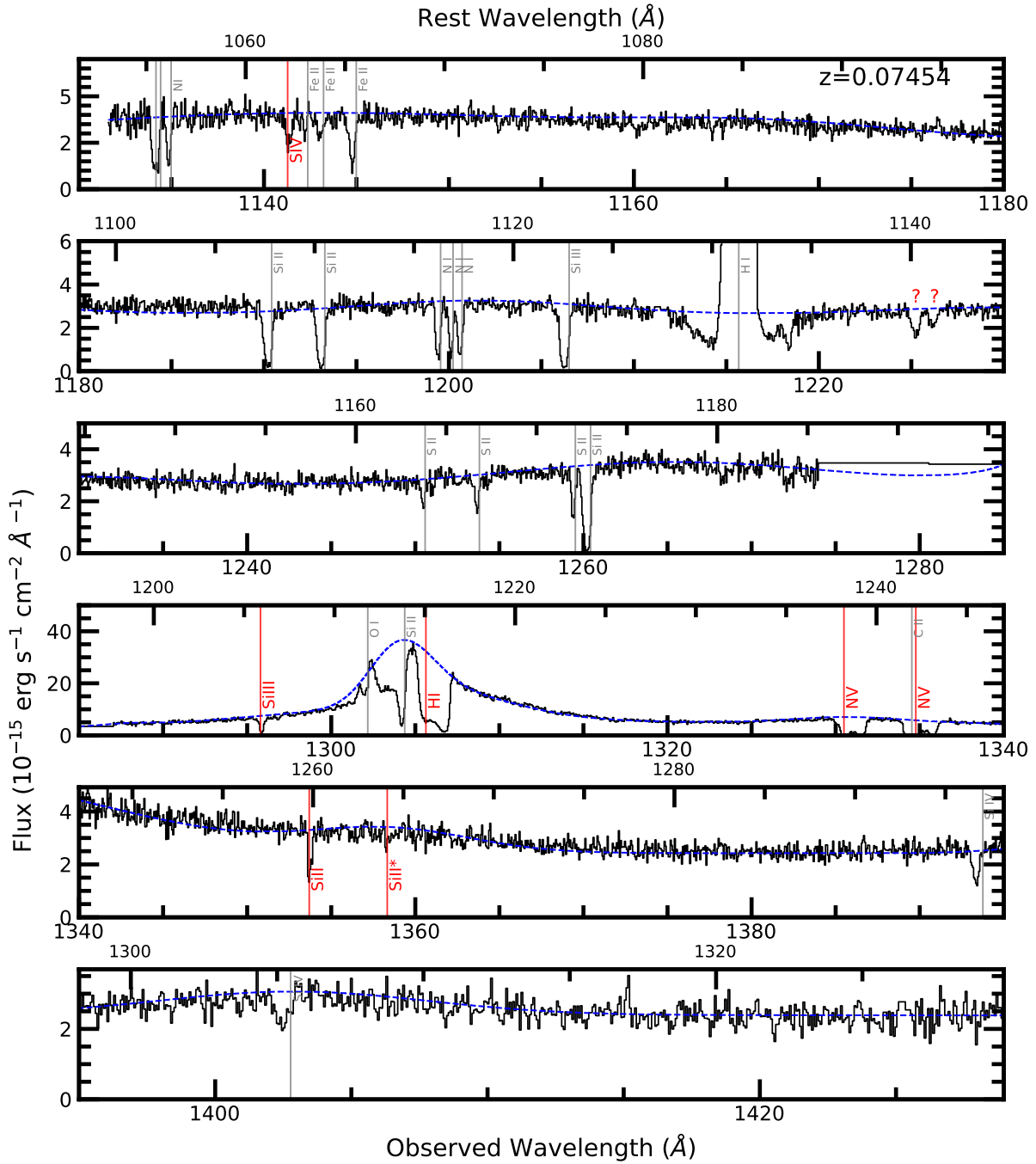While the above solution satisfies all the constraints, we exam-

**Figure 1.** The spectrum of J1429+4518 observed by the HST/COS in Sep 2021(Putman et al. 2020). The absorption features of the outflow system with a velocity of −151 km/s are marked with red lines, while the grey lines show the absorption from the interstellar medium (ISM). The dashed blue line shows our continuum emission model. The question marks indicate some absorption lines that we could not identify (we confirm they are not CIV resulting from an intervening system).
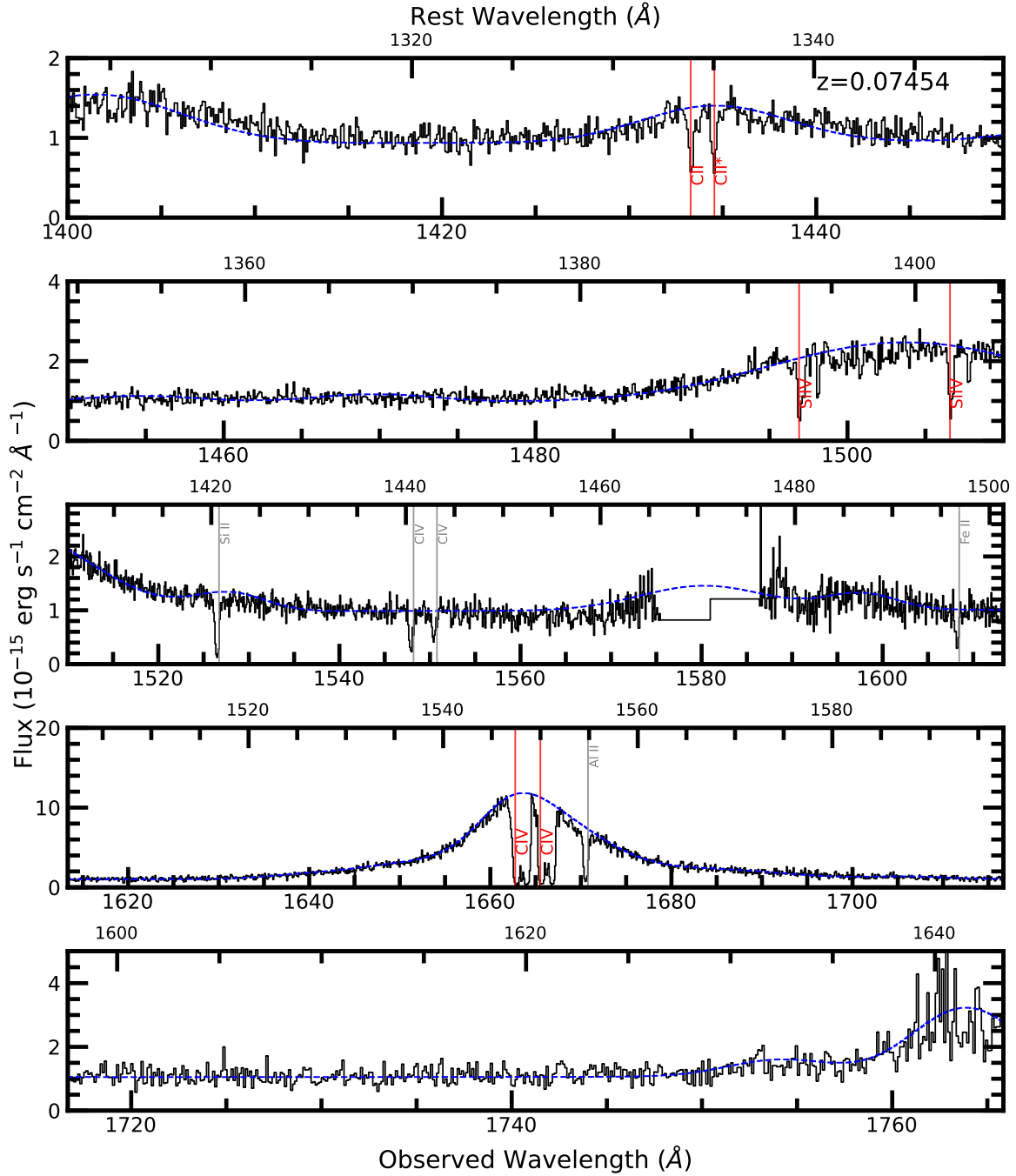
**Figure 2.** Same as Fig.1 but the data are from HST/COS observations in Dec 2021 (Putman et al. 2020). Note that since the C IV lines are black at the bottom, the covering fraction of the NAL outflow is estimated to be 1.0.

ined the dependency of the results on the SED and metalicity. For this purpose, we repeated the same process of prediction $N_H$ and $U_H$ using another two SEDs, namely the MF87 SED (Mathews & Ferland 1987), and UV-soft SED (Dunn et al. 2010). For all three SEDs, we have also investigated the effects of super-solar metalicity ($Z=4.68Z_\odot$) (Ballero et al. 2008; Miller et al. 2020b). The lower

panel of Fig. 5 shows the effects of different SEDs and super-solar metalicity on the results. In this Figure, each solid line belongs to the calculations considering a solar metalicity while dashed lines are resulted from a super-solar metalicity. These results show that using MF87 and UV-soft SEDs results in a slightly smaller $\chi^2$ (2.3 and 1.5, respectively). However, as discussed by Arav et al. (2013), we
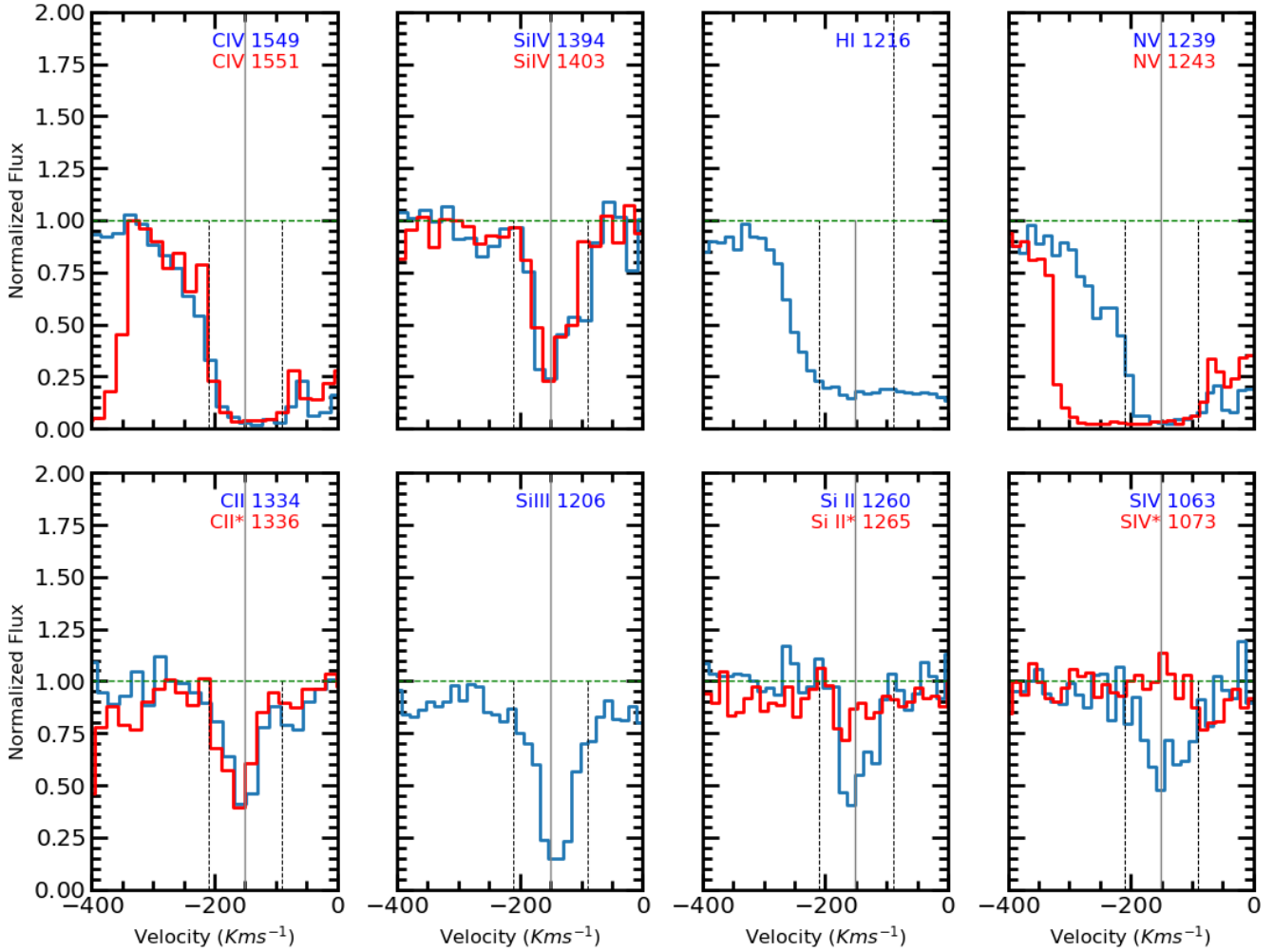
**Figure 3.** Normalized flux versus velocity for blue-shifted absorption lines detected in the spectrum of J1429+4518. The horizontal green dashed horizontal line shows the continuum level, and the vertical black dashed lines show the region between -210 and -90 km s$^{-1}$. The vertical solid black line indicates the centroid velocity of $v_{centroid}=-151$ kms$^{-1}$.

prefer to continue using HE0238 SED since it extends quite far into the extreme UV rest (EUV) wavelength range.

### 3.3 Determining the electron number density and the distance of the outflow from the central source

#### 3.3.1 Electron Number Density

We ran a model of Cloudy using HE0238 SED and the $N_H$ and $U_H$ values to predict the outflow's temperature. This simulation resulted in a temperature of T$\approx$14000 K. Assuming this temperature, we used Chianti 9.0.1 atomic database (Dere et al. 1997, 2019) to estimate the abundance ratios of excited state to the resonance state for Si II, C II, and S IV as a function of electron number density ($n_e$). Fig. 6 illustrates the results. Since Si II's absorptions in both excited and resonance states were reliably measured (section 3.1.5), we took its ratio as a diagnostics for the electron number density of the outflow (blue curve in Fig. 6). These considerations result in log $n_e$= $2.75^{+0.20}_{-0.25}$ [cm$^{-3}$]. As described in Osterbrock & Ferland (2006) and for a highly ionized plasma, $n_e \approx 1.2 n_H$, resulting in log $n_H$= $2.67^{+0.20}_{-0.25}$ [cm$^{-3}$]. We have also used C II and S IV to predict lower and

higher limits for $n_e$ (details in sections 3.1.3 and 3.1.6, respectively). These upper and lower constraints on $n_e$ are fully consistent with the Si II*/Si II measurement.

#### 3.3.2 Location of the Outflow

Once $N_H$, $n_H$, and $U_H$ are known, we can use equation 14.4 from Osterbrock & Ferland (2006) to extract the location of the outflow:

$$U_H \equiv \frac{Q(H)}{4\pi R^2 c \, n_H} \Rightarrow R = \sqrt{\frac{Q(H)}{4\pi c \, n_H U_H}} \qquad (3)$$

In which Q(H) [s$^{-1}$] is the number of hydrogen-ionizing photons emitted by the central object per second, R is the distance between the outflow and the central source, $n_H$ is the hydrogen density and c is the speed of light.

To calculate R, we must first calculate the number of hydrogen-ionizing photons Q(H). To do so, we followed several steps explained below (please refer to the works done by Miller et al. (2020a), Byun et. al (2022a,b), and Walker et. al (2022)):

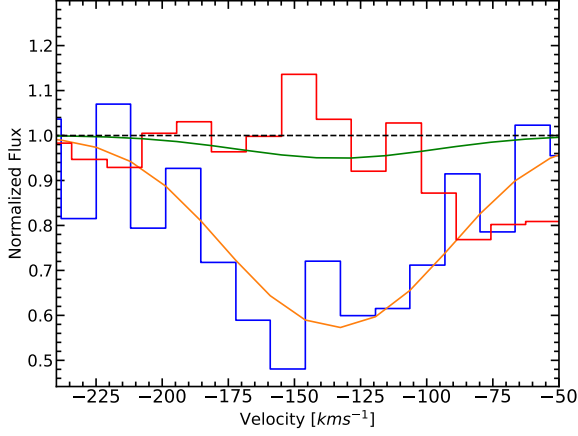• First, We scaled the SED of HE0238 to match the continuum

**Figure 4.** Gaussian modeling (green) of the S IV* $\lambda1073$ Å absorption trough, created by fitting S IV $\lambda1063$ Å line (orange) and using its shape as a template, where we have allowed the optical depth to adjust within $3\sigma$ error range. The horizontal dashed line shows the continuum level.

flux of J1429+4518 at observed wavelength of $\lambda=1350$Å. Based on the HST observations we are using in this paper, at the mentioned wavelength $F_\lambda \approx 3 \times 10^{-15}$ erg s$^{-1}$ cm$^{-2}$ Å$^{-1}$.

• Then, we integrated over the scaled SED for all energies above 1 Ryd (Hydrogen ionization potential) to get a value of $1.2^{+0.1}_{-0.1} \times 10^{54}$ s$^{-1}$ for Q(H) and a bolometric luminosity of $L_{bol}= 2.13^{+0.2}_{-0.2} \times 10^{44}$ erg s$^{-1}$.

• Finally, using these values and equation 3, we predict that the outflow system is located at a distance of R$\approx275^{+53}_{-46}$ pc from the source.

### 3.4 Black hole mass and outflow's energetics

#### 3.4.1 Black Hole mass and the Eddington luminosity

To get an estimate of the outflow's energetics, including its mass-loss rate and the kinetic luminosity, we need to get a hand on the mass of central BH and its Eddington luminosity first.

In 2006, Vestergaard & Peterson showed that C IV emission line could be used to measure the mass of the BH via this equation:

$$\log M_{BH}(\text{C IV}) = \log(\left[\frac{\text{FWHM(C IV)}}{1000\text{kms}^{-1}}\right]^2 \left[\frac{\lambda L_\lambda(1350)}{10^{44}\text{ergs}^{-1}}\right]^{0.53}) \quad (4)$$

Later in 2017, Coatman et al. revised equation 4 as below:

$$M_{BH}(\text{C IV, Corr.}) = 10^{6.71}\left[\frac{\text{FWHM(C IV, Corr.)}}{1000\text{kms}^{-1}}\right]^2 \times$$
$$\left[\frac{\lambda L_\lambda(1350)}{10^{44}\text{ergs}^{-1}}\right]^{0.53} \quad (5)$$

where:

$$\text{FWHM(C IV, Corr.)} = \frac{\text{FWHM(C IV, Meas.)}}{(0.41 \pm 0.02)\frac{\text{C IV blueshift}}{1000\text{kms}^{-1}} + (0.62 \pm 0.04)} \quad (6)$$

As shown in Fig. 2, we can easily identify the C IV emission and use its FWHM to achieve the mass of the black hole. Fig. 7 shows our Gaussian model to fit the spectra at C IV region, in which we
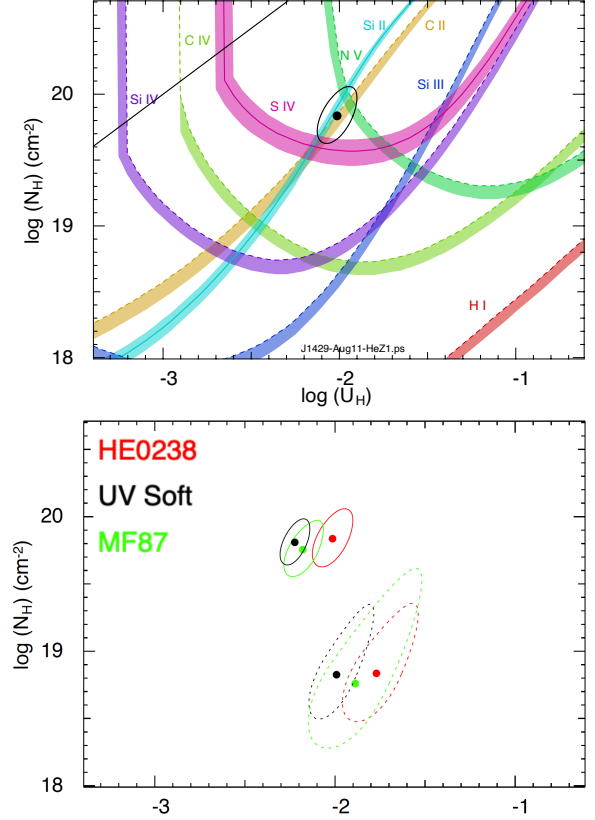


**Figure 5.** Top panel: single phase photoionization solution for the absorption outflow system. Each coloured contour indicates the ionic column densities consistent with the observations (available in Table 1), assuming the HE0238 SED and solar metallicity. Solid lines within the contours show the ionic column densities taken as measurements, while dashed lines contours belong to lower limits. The shaded bands are the uncertainties added for each contour. The black circle shows the best $\chi^2$-minimization solutions. Bottom Panel: The photoionization solution for a total of six models, including three SEDs (HE0238, MF87, and UV–soft) and two metallicities for each: solar metallicity and super-solar metallicity, for a total of six models.

have modeled the C IV emission with a single Gaussian. Based on this Figure, the FWHM is measured to be $\approx3100$ km s$^{-1}$ for the C IV emission line. We also measured an average flux of $1\times10^{-15}$ erg s$^{-1}$ cm$^{-2}$ Å$^{-1}$ for $\lambda_{rest}=1350$Å, which for our narrow outflow system results in $\lambda L_\lambda=1.16\times10^{42}$ erg s$^{-1}$. Using these values in the equation 6 & 5, we get a black hole mass of $M_{BH}=7.5\times10^6$M$_\odot$, resulting in an Eddington luminosity of $L_{Edd}=8.8\times10^{44}$ erg s$^{-1}$.

#### 3.4.2 Outflow's Energetics

Using outflow's R and $N_H$ obtained above, we can estimate the mass-loss rate and the kinetic luminosity of the outflow using the following equations(Borguet et al. 2012b):

$$\dot{M} \simeq 4\pi\Omega RN_H\mu m_p v \quad (7)$$

$$\dot{E}_K \simeq \frac{1}{2}\dot{M}v^2 \quad (8)$$

In equation 7, $\mu = 1.4$ is the mean atomic mass per proton, v is the velocity of the outflow, and $m_p$ is the mass of a proton (Borguet et al. 2012a). In the mentioned equation, $\Omega$ is the global covering
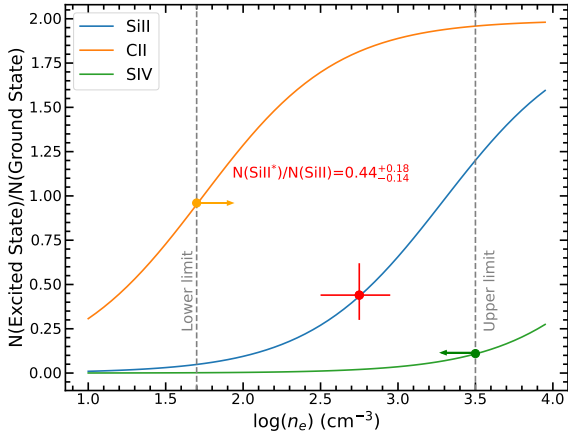
**Figure 6.** The excited state to resonance state column density ratio vs. the electron number density from Chianti atomic database. We have shown the calculated value from our modeling and marked its corresponding electron number density by a vertical dashed line. Please note that these results are sensitive to the temperature, and to produce this plot, we assumed T=14000 K.
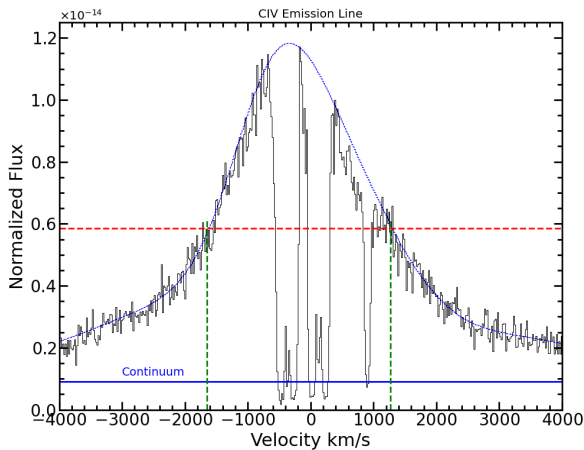


**Figure 7.** C IV emission line region. The blue line shows our Gaussian fit to the emission spectra. The Red dashed line indicates where the half maximum is, while the green dashed lines show the full width of the half maximum. The continuum level is shown in the Figure, and it is subtracted for the purpose of FWHM determination.

factor defined as the percentage of the source covered by the outflow in all directions (not only line-of-sight). We assume $\Omega = 0.5$ as Misawa et al. (2007b) explain that intrinsic NALs are observed in at least 50% of AGNs. In an earlier study published in 2003, Vestergaard discusses more than half of the AGNs embed NALs. All these studies are in agreement with the 50-70% population ratio of NALs among Seyfert 1 galaxies as reported by Crenshaw et al. (1999). Assuming all these values and solving equations 7 and 8 for the mass-loss rate and the kinetic luminosity results in $\dot{M}=0.22^{+0.09}_{-0.06} M_\odot yr^{-1}$ and $\log \dot{E_K}=39.3^{+0.1}_{-0.2}$ [erg s$^{-1}$]. Table 2 summarizes all these results along with the results from section 3.

| | |
|---|---|
| $\log N_H$ [cm$^{-2}$] | $19.84^{+0.20}_{-0.20}$ |
| $\log U_H$ [dex] | $-2.0^{+0.1}_{-0.1}$ |
| $\log n_e$ [cm$^{-3}$] | $2.75^{+0.20}_{-0.20}$ |
| R [pc] | $275^{+53}_{-46}$ |
| $\dot{M}$ [$M_\odot yr^{-1}$] | $0.22^{+0.09}_{-0.06}$ |
| $\log \dot{E_K}$ [erg s$^{-1}$] | $39.3^{+0.1}_{-0.2}$ |
| $\dot{E_K}/L_{Edd}$ | $2.0^{+0.9}_{-0.7} \times 10^{-6}$ |
| $\dot{E_K}/L_{Bol}$ | $8.5^{+3.0}_{-2.0} \times 10^{-6}$ |

**Table 2.** Physical properties of the narrow absorption line outflow system

As reported in Table 2, the outflow system's kinetic luminosity ratio to the source's Eddington luminosity is $\approx 0.0002\%$. Hopkins & Elvis (2010) explain that an outflow system must have a $\dot{E_K}/L_{Edd}$ of at least $\approx 0.5\%$ to contribute to the AGN outflow, verifying that the NAL outflow system identified here does not contribute to AGN feedback processes.

It is worth mentioning that if we take the redshift considerations into account (Section 2.1) and assume that the outflow has a velocity of approximately $-195$ km s$^{-1}$, then $\dot{M}=0.27 M_\odot yr^{-1}$ and $\log \dot{E_K}=39.5$[erg s$^{-1}$]. Based on these values, the outflow system's kinetic luminosity ratio to the source's Eddington luminosity would be $\approx 0.0004\%$. This indicates that for the [OIII]-based redshift, the above discussion remains valid, and this outflow contributes minimally or not at all to the AGN feedback process.

## 4 DISCUSSION

### 4.1 The thermal stability curve

When gas is photoionized, it will reach the equilibrium defined by an ionization parameter (Tarter et. al 1969; Kallman & Bautista 2001):

$$\xi \equiv \frac{L_{\text{ion}}}{n_H r^2} [\text{erg cm s}^{-1}] \tag{9}$$

and a specific temperature. This equilibrium arises due to the interplay between various heating and cooling mechanisms that depend on the gas's physical and chemical attributes and the characteristics of the intrinsic radiation of the source.

It is common to represent these balanced states on a stability curve, depicted in a diagram with temperature (T) on the vertical axis and the ratio of $\xi/T$ on the horizontal axis (for example, Krolik et. al (1981)). When we assume that L/n(H)r$^2$ remains constant , the latter parameter, $\frac{\xi}{T} \propto \frac{p_{rad}}{p_{gas}}$, indicates the gas pressure. The thermal stability curve (S-curve) for J1429+4518 is produced using Cloudy and is shown in Fig. 8. To create the stability curve, we have used the previously mentioned HE0238 SED and the outflow's characteristics are adopted from Table 2. In this Figure, the region on the left-hand side of the curve is dominated by cooling processes, while heating processes dominate the right-hand side. A positive slope on the S-curve happens when an increase in T (due to an isobaric perturbation)
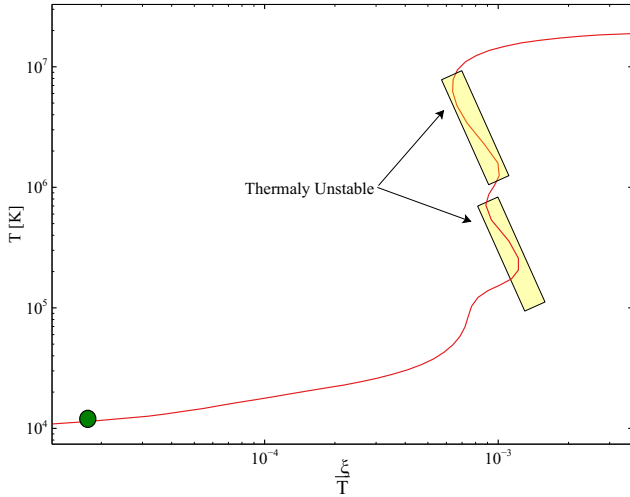
**Figure 8.** The photoionization stability curve (s-curve) for J1429+4518. The green circle indicates the narrow absorption outflow system discussed in this paper. Yellow rectangles indicate the negative-slope regions, meaning any gas with those characteristics would be unstable.

will move the gas to the cooling region and so revert the gas to the same equilibrium state. Such equilibrium states are considered to be thermally stable. The green circle in Fig. 8 indicates where our narrow absorption line outflow is located regarding the stability. Based on this plot, the outflow is on the positive slope and hence it is assumed to be thermally stable.

### 4.2 The Importance of the NALs

Hamann et al. (2011) explain that to understand AGN outflows better, we need clearer information about the different types of outflows, including NAL outflows. For a while now, there has been an ongoing discussion about whether the NALs and BALs (Broad Absorption Lines) have any connection or relationship (Weymann et al. 1979). Furthermore, there's an ongoing debate about how these associated NALs and BALs might fit into the overall development or evolution of AGNs (Briggs et al. 1984; Hamann et al. 2001).

It's not straightforward to detect NAL outflows because they're hard to identify: most narrow lines we see in AGN spectra come from unrelated cosmic gas, not from the AGN themselves. However, some studies suggest that a significant part of these narrow absorption lines actually come from AGN outflows (e.g. Nestor et. al 2008; Wild et al. 2008; Richards 2001).

### 4.3 Similarity to Milky Way Outflows

The narrow absorption line outflow system in J1429+4518 shows some remarkable similarity to the two bipolar lobe outflows observed in the Milky Way by XMM-Newton and Chandra (see Ponti et al. (2019), figure 1). One of these lobe outflows extends up to 160 pc from the Galactic Center (GC) in the northern direction. The second lobe, situated to the south, extends even further, reaching beyond the southern Fermi Bubble's base and spanning approximately 250 pc (Veilleux et al. 2020). Notably, the distances from their central source align closely with the 275 pc measured for our study's NAL outflow system. Furthermore, their kinematic luminosities are estimated at $\log \dot{E}_K$=39.6 [erg s$^{-1}$] (Ponti et al. 2019)—merely 0.3

dex larger than that of our outflow system—these similarities are striking. Finally, the comparability of the Milky Way's black hole mass ($M_{BH}$=4.15×10$^6$M$_\odot$; GRAVITY Collaboration et al. (2019)) with that of J1429+4518 ($M_{BH}$=6.7×10$^6$M$_\odot$) along with the mentioned similarities in the outflow's measurements, suggest a common origin for the two outflows. It's worth noting that other outflows in the Milky Way are located farther away or have much larger kinetic luminosity(Veilleux et al. 2020).

## 5 CONCLUSIONS

In this paper, we analysed two datasets from HST/COS 2021 observations of Seyfert 1 galaxy J1429+4518. We successfully identified a narrow absorption line outflow system located ~275 pc away from the central source. This outflow was identified through narrow absorption troughs of C IV, Si IV, N IV, Lyα, C II, C II*, Si II, Si II*, Si III, and S IV. We measured the centroid velocity of the outflow system to be –151 km s$^{-1}$ and extracted the ionic column densities of the absorption lines using the AOD method.

As the next step, measured ionic column densities were used to determine the total hydrogen column density ($\log N_H$=19.84 erg s$^{-1}$) and the ionization state ($\log U_H$=-2.0) of the NAL outflow. This was done by using $\chi^2$-minimization solutions and performing Cloudy simulations. We also used the ratio of the ionic column densities of Si II* to Si II for measuring the electron number density ($\log n_e$=2.75 cm$^{-3}$) and hence its hydrogen density. Having the hydrogen density enabled us to estimate the outflow location mentioned above. We followed all these calculations by estimating the energetics of the outflow: this outflow has a kinetic luminosity of $\log \dot{E}_K$=39.3[erg s$^{-1}$] and its mass-loss rate is measured to be $\dot{M}$=0.22$M_\odot yr^{-1}$.

The NAL outflow of J1429+4518 is thermally stable, but it does not contribute to AGN feedback processes since its kinetic luminosity is only ≈ 0.00025% of the Eddington luminosity of the central source. Finally, we note that this NAL outflow exhibits a striking similarity to the two bipolar lobe outflows detected in the Milky Way through observations conducted by XMM-Newton and Chandra. The similarities in their energetics and location, and having central black holes with similar masses, strongly suggest that these outflows might have a common origin.

## DATA AVAILABILITY

The data of J1429+4518 described in this paper may be obtained from the MAST archive at `https://dx.doi.org/10.17909/mzeb-fm44`

## REFERENCES

Arav N., Korista K. T., de Kool M., Junkkarinen V. T., Begelman M. C., 1999a, ApJ, 516, 27. doi:10.1086/307073

Arav N., Becker R. H., Laurent-Muehleisen S. A., Gregg M. D., White R. L., Brotherton M. S., de Kool M., 1999b, ApJ, 524, 566. doi:10.1086/307841

Arav N., Brotherton M. S., Becker R. H., Gregg M. D., White R. L., Price T., Hack W., 2001, ApJ, 546, 140. doi:10.1086/318244

Arav N., Korista K. T., de Kool M., 2002, ApJ, 566, 699. doi:10.1086/338113

Arav N., Kaastra J., Kriss G. A., Korista K. T., Gabel J., Proga D., 2005, ApJ, 620, 665. doi:10.1086/425560

Arav N., Borguet B., Chamberlain C., Edmonds D., Danforth C., 2013, MNRAS, 436, 3286. doi:10.1093/mnras/stt1812

Arav N., Liu G., Xu X., Stidham J., Benn C., Chamberlain C., 2018, ApJ, 857, 60. doi:10.3847/1538-4357/aab494

Astropy Collaboration, Robitaille T. P., Tollerud E. J., Greenfield P., Droettboom M., Bray E., Aldcroft T., et al., 2013, A&A, 558, A33. doi:10.1051/0004-6361/201322068

Astropy Collaboration, Price-Whelan A. M., Sipőcz B. M., Günther H. M., Lim P. L., Crawford S. M., Conseil S., et al., 2018, AJ, 156, 123. doi:10.3847/1538-3881/aabc4f

Ballero S. K., Matteucci F., Ciotti L., Calura F., Padovani P., 2008, A&A, 478, 335. doi:10.1051/0004-6361:20078663

Barlow T. A., Hamann F., Sargent W. L. W., 1997, ASPC, 128, 13. doi:10.48550/arXiv.astro-ph/9705048

Bennett C. L., Larson D., Weiland J. L., Hinshaw G., 2014, ApJ, 794, 135. doi:10.1088/0004-637X/794/2/135

Briggs F. H., Turnshek D. A., Wolfe A. M., 1984, ApJ, 287, 549. doi:10.1086/162713

Borguet B. C. J., Edmonds D., Arav N., Dunn J., Kriss G. A., 2012a, ApJ, 751, 107. doi:10.1088/0004-637X/751/2/107

Borguet B. C. J., Edmonds D., Arav N., Benn C., Chamberlain C., 2012b, ApJ, 758, 69. doi:10.1088/0004-637X/758/1/69

Byun D., Arav N., Walker A., 2022a, MNRAS, 516, 100. doi:10.1093/mnras/stac2194

Byun D., Arav N., Hall P. B., 2022b, MNRAS, 517, 1048. doi:10.1093/mnras/stac2638

Byun D., Arav N., Hall P. B., 2022c, ApJ, 927, 176. doi:10.3847/1538-4357/ac503d

Zhi-Fu Chen and Yi-Ping Qin 2013 ApJ 777 56 doi:10.1088/0004-637X/777/1/56

Chen Z.-F., Pan D.-S., 2017, ApJ, 848, 79. doi:10.3847/1538-4357/aa8d66

Chen Z.-F., Pang T.-T.,He b., Huang Y., 2018, ApJS,236, 39. doi:10.3847/1538-4365/aabcd4

Chen Z.-F., Huang W.-R., Pang T.-T., Huang H.-Y., Pan D.-S., Yao M., Nong W.-J., et al., 2018, ApJS, 235, 11. doi:10.3847/1538-4365/aaaaec

Chen Z.-F., Yi S.-X., Pang T.-T., Chen Z.-G., Gui R.-J., Wang Z.-W., Mo X.-H., et al., 2019, ApJS, 244, 36. doi:10.3847/1538-4365/ab41fe

Chen Z.-F., Qin H.-C., Gui R.-J., Yi S.-X., Chen Z.-G., Gao Y.-C., Pang T.-T., et al., 2020, ApJS, 250, 3. doi:10.3847/1538-4365/aba520

Chen Z., He Z., Ho L. C., Gu Q., Wang T., Zhuang M., Liu G., et al., 2022, NatAs, 6, 339. doi:10.1038/s41550-021-01561-3

Coatman L., Hewett P. C., Banerji M., Richards G. T., Hennawi J. F., Prochaska J. X., 2017, MNRAS, 465, 2120. doi:10.1093/mnras/stw2797

Crenshaw D. M., Kraemer S. B., Boggess A., Maran S. P., Mushotzky R. F., Wu C.-C., 1999, ApJ, 516, 750. doi:10.1086/307144

de Kool M., Korista K. T., Arav N., 2002, ApJ, 580, 54. doi:10.1086/343107

Dere K. P., Landi E., Mason H. E., Monsignori Fossi B. C., Young P. R., 1997, A&AS, 125, 149. doi:10.1051/aas:1997368

Dere K. P., Del Zanna G., Young P. R., Landi E., Sutherland R. S., 2019, ApJS, 241, 22. doi:10.3847/1538-4365/ab05cf

Dunn J. P., Bautista M., Arav N., Moe M., Korista K., Costantini E., Benn C., et al., 2010, ApJ, 709, 611. doi:10.1088/0004-637X/709/2/611

Ferland G. J., Chatzikos M., Guzmán F., Lykins M. L., van Hoof P. A. M., Williams R. J. R., Abel N. P., et al., 2017, RMxAA, 53, 385. doi:10.48550/arXiv.1705.10877

Gabel J. R., Crenshaw D. M., Kraemer S. B., Brandt W. N., George I. M., Hamann F. W., Kaiser M. E., et al., 2003, ApJ, 583, 178. doi:10.1086/345096

GRAVITY Collaboration, Abuter R., Amorim A., Bauböck M., Berger J. P., Bonnet H., Brandner W., et al., 2019, A&A, 625, L10. doi:10.1051/0004-6361/201935656

Hamann, F. W., Barlow, T. A., Chaffee, F. C., Foltz, C. B., Weymann, R. J. 2001. High-Resolution Keck Spectra of the Associated Absorption Lines in 3C 191. The Astrophysical Journal 550, 142–152. doi:10.1086/319733

Hamann F., Kanekar N., Prochaska J. X., Murphy M. T., Ellison S., Malec A. L., Milutinovic N., et al., 2011, MNRAS, 410, 1957. doi:10.1111/j.1365-2966.2010.17575.x

Harris C. R., Millman K. J., van der Walt S. J., Gommers R., Virtanen P., Cournapeau D., Wieser E., et al., 2020, Natur, 585, 357. doi:10.1038/s41586-020-2649-2

He Z., Liu G., Wang T., et al. 2022, Science Advances, 8, eabk3291

Hopkins P. F., Elvis M., 2010, MNRAS, 401, 7. doi:10.1111/j.1365-2966.2009.15643.x

Hunter J. D., 2007, CSE, 9, 90. doi:10.1109/MCSE.2007.55

Itoh D., Misawa T., Horiuchi T., Aoki K., 2020, MNRAS, 499, 3094. doi:10.1093/mnras/staa2793

Kallman T., Bautista M., 2001, ApJS, 133, 221. doi:10.1086/319184

Krolik J. H., McKee C. F., Tarter C. B., 1981, ApJ, 249, 422. doi:10.1086/159303

Mathews W. G., Ferland G. J., 1987, ApJ, 323, 456. doi:10.1086/165843

Miller T. R., Arav N., Xu X., Kriss G. A., Plesha R. J., Benn C., Liu G., 2018, ApJ, 865, 90. doi:10.3847/1538-4357/aad817

Miller T. R., Arav N., Xu X., Kriss G. A., Plesha R. J., 2020a, ApJS, 247, 39. doi:10.3847/1538-4365/ab5967

Miller T. R., Arav N., Xu X., Kriss G. A., Plesha R. J., 2020b, ApJS, 247, 41. doi:10.3847/1538-4365/ab5969

Miller T. R., Arav N., Xu X., Kriss G. A., Plesha R. J., 2020c, ApJS, 249, 15. doi:10.3847/1538-4365/ab94b9

Misawa T., Charlton J. C., Eracleous M., Ganguly R., Tytler D., Kirkman D., Suzuki N., et al., 2007a, ApJS, 171, 1. doi:10.1086/513713

Misawa T., Eracleous M., Charlton J. C., Ganguly R., Tytler D., Kirkman D., Suzuki N., et al., 2007b, ASPC, 373, 291. doi:10.48550/arXiv.astro-ph/0612028

Nestor D., Hamann F., Rodriguez Hidalgo P., 2008, MNRAS, 386, 2055. doi:10.1111/j.1365-2966.2008.13156.x

Osterbrock D. E., Ferland G. J., 2006, agna.book

Ponti G., Hofmann F., Churazov E., Morris M. R., Haberl F., Nandra K., Terrier R., et al., 2019, Natur, 567, 347. doi:10.1038/s41586-019-1009-6

Putman M. E., Burchett J. N., Emerick A., Kirby E., McQuinn K. B. W., Oppenheimer B. D., Werk J. K., et al., 2020, hst..prop, 16301

Reback J., McKinney W., jbrockmendel, Van den Bossche J., Augspurger T., Cloud P., Hawkins S., et al., 2021, zndo

Richards G. T., 2001, ApJS, 133, 53. doi:10.1086/319183

Savage B. D., Sembach K. R., 1991, ApJ, 379, 245. doi:10.1086/170498

Shen Y., Richards G. T., Strauss M. A., Hall P. B., Schneider D. P., Snedden S., Bizyaev D., et al., 2011, ApJS, 194, 45. doi:10.1088/0067-0049/194/2/45

Shen Y., Ménard B., 2012, ApJ, 748, 131. doi:10.1088/0004-637X/748/2/131

Silk J., Rees M. J., 1998, A&A, 331, L1. doi:10.48550/arXiv.astro-ph/9801013

Scannapieco E., Oh S. P., 2004, ApJ, 608, 62. doi:10.1086/386542

Spitzer L., 1968, dms..book

Tarter C. B., Tucker W. H., Salpeter E. E., 1969, ApJ, 156, 943. doi:10.1086/150026

Vayner A., Wright S. A., Murray N., Armus L., Boehle A., Cosens M., Larkin J. E., et al., 2021, ApJ, 919, 122. doi:10.3847/1538-4357/ac0f56

Veilleux S., Maiolino R., Bolatto A. D., Aalto S., 2020, A&ARv, 28, 2. doi:10.1007/s00159-019-0121-9

Vestergaard M., 2003, ApJ, 599, 116. doi:10.1086/379159

Vestergaard M., Peterson B. M., 2006, ApJ, 641, 689. doi:10.1086/500572

Virtanen P., Gommers R., Oliphant T. E., Haberland M., Reddy T., Cournapeau D., Burovski E., et al., 2020, NatMe, 17, 261. doi:10.1038/s41592-019-0686-2

Walker A., Arav N., Byun D., 2022, MNRAS, 516, 3778. doi:10.1093/mnras/stac2349

Weymann R. J., Williams R. E., Peterson B. M., Turnshek D. A., 1979, ApJ, 234, 33. doi:10.1086/157470

Wild V., Kauffmann G., White S., York D., Lehnert M., Heckman T., Hall P. B., et al., 2008, MNRAS, 388, 227. doi:10.1111/j.1365-2966.2008.13375.x

Xu X., Arav N., Miller T., Benn C., 2018, ApJ, 858, 39. doi:10.3847/1538-4357/aab7ea

Xu X., Arav N., Miller T., Benn C., 2019, ApJ, 876, 105. doi:10.3847/1538-4357/ab164e

Yuan F., Yoon D., Li Y.-P., Gan Z.-M., Ho L. C., Guo F., 2018, ApJ, 857, 121. doi:10.3847/1538-4357/aab8f8

This paper has been typeset from a TEX/LATEX file prepared by the author.